

## Numerical investigation of the three-dimensional pressure distribution in Taylor Couette flow

Item Type	Journal article
Authors	Adebayo, David Shina;Rona, A
Citation	Adebayo, D. S. and Rona, A. (2017) Numerical investigation of the three-dimensional pressure distribution in Taylor Couette flow,
DOI	<a href="https://doi.org/10.1115/1.4037083">10.1115/1.4037083</a>
Publisher	ASME International
Journal	Journal of Fluids Engineering
Download date	2026-03-16 23:23:48
License	<a href="https://creativecommons.org/licenses/by/4.0/">https://creativecommons.org/licenses/by/4.0/</a>
Link to Item	<a href="http://hdl.handle.net/2436/622806">http://hdl.handle.net/2436/622806</a>

## **Numerical investigation of the three-dimensional pressure distribution in Taylor Couette flow**

**David Shina Adebayo**

*University of Leicester*

*Department of Engineering, University Road,*

*Leicester, LE1 7RH, U.K.*

*dsa5@le.ac.uk*

**Aldo Rona**

*University of Leicester*

*Department of Engineering, University Road,*

*Leicester, LE1 7RH, U.K.*

*ar45@le.ac.uk*

### **ABSTRACT**

*An investigation is conducted on the flow in a moderately wide gap between an inner rotating shaft and an outer coaxial fixed tube, with stationary end-walls, by three dimensional Reynolds Averaged Navier-Stokes (RANS) Computational Fluid Dynamics, using the realizable  $k - \varepsilon$  model. This approach provides three-dimensional spatial distributions of static and of dynamic pressure that are not directly measurable in experiment by conventional non-intrusive optics-based techniques. The non-uniform pressure main features on the axial and meridional planes appear to be driven by the radial momentum equilibrium of the flow, which is characterized by axisymmetric Taylor vortices over the Taylor number range  $2.35 \times 10^6 \leq Ta \leq 6.47 \times 10^6$ . Regularly spaced static and dynamic pressure maxima on the stationary cylinder wall follow the axial stacking of the Taylor vortices and line up with the vortex induced radial outflow documented in previous work. This new detailed understanding has potential for application to the design of a vertical turbine pump head. Aligning the location where the gauge static pressure maximum occurs with the central axis of the delivery*

*pipe could improve the head delivery, the pump mechanical efficiency, the system operation, and control costs.*

## 1.0 Introduction

Many scientific and industrial applications feature a flow in the annulus of two concentric rotating shafts. This study therefore stands to benefit the many applications and deliver a high research impact. In the case in which the inner shaft is rotating and the outer tube is kept fixed, Taylor vortices [1, 2, 3, 4] can develop in the annulus between the two coaxial shafts, due to an unstable pressure gradient acting on the fluid particles. Over a certain range of Taylor numbers,  $Ta$ , the developed Taylor vortices remain stable and axisymmetric. As the Taylor number increases beyond this range, a small mean axial pressure gradient is superimposed and three-dimensional secondary flows with vortex structures are generated. The modelling and the analysis of these flow patterns provide information about heat and mass transfer rates, pressure distributions, and axial mixing in important industrial applications, such as liquid-liquid extraction [5, 6], exhaust fans, synthesis of silica particles [7], emulsion polymerization [8], bio-reactions [9], as well as heterogeneous catalytic reactions [10]. The applications that currently represent the most significant economic and societal impacts are submerged pumps for water wells and vertical turbine pumps, where the impeller at the bottom of the well is mechanically driven by a shaft connected to an electric motor.

The energy used worldwide by pumps for lifting and moving fluids is about 10% of the total world energy consumption [11], which is a very sizeable value, given the  $15.750 \times 10^{15}$  Wh of energy used worldwide in 2013 [12]. The cost of pumping, specifically of water, has the highest impact on the economy of developing countries, in particular, in the sub-Saharan region. The understanding of the pressure distribution in a rotating system can help to improve the design of current pumps, reducing the financial and environmental cost of pumping operations.

This research therefore contributes to the global challenge identified by the Research Councils UK (RCUK) of achieving a more sustainable energy use and to the UK government Official Development

Assistance (ODA) to developing countries by promoting technology for the provision of affordable water.

The experiments by Mallock [1, 2] and by Couette [13] provided early insight into the flow in the annulus of two concentric independently rotating shafts. These investigators observed the development of flow instabilities, which were first explained by Taylor [3] using perturbation theory. Since then, many other researchers, including Jeffreys [14], Chandrasekhar [4, 15], Di Prima [16], Andereck et al. [17], Coles [18], Koschmieder [19], Liao et al. [20], Czarny et al. [21], and Serre et al. [22], have used experiments, numerical models and analytical techniques to unravel the complexities of the Taylor instability that characterizes the flow between rotating cylinders. These researchers established that the complex steady and unsteady flow patterns between concentric independently rotating cylinders are due to small perturbations. They also concluded that Taylor number,  $Ta$ , [3, 16] is a major parameter in determining the flow regime and pattern that develop in the clearance between two coaxial rotating shafts.

There are four main controlling parameters for the case in which the outer tube is fixed and the inner shaft rotates, as in this study. These are:

$$(1) \eta = R_i/R_o;$$

$$(2) d = R_o - R_i;$$

$$(3) \Omega;$$

$$(4) \nu;$$

where  $R_i$ ,  $R_o$ ,  $\Omega$ , and  $\nu$  are defined in the nomenclature. The Taylor number  $Ta$ , is related to these controlling parameters by

$$Ta = \frac{2\eta^2 d^4}{1 - \eta^2} \left( \frac{\Omega}{\nu} \right)^2 \quad (1)$$

A brief overview of the literature shows that many experimental investigations have been conducted on the flow pattern in the meridional plane, especially on the in-plane velocity. For

instance, Adebayo and Rona [23, 24] and Wereley and Lueptow [25, 26] used non-intrusive optical measurement techniques for measuring the in-plane velocity. These measurements were limited only to the meridional plane, due to the challenge of capturing the flow pattern in the axial plane, which presents a more difficult optical access. Furthermore, the static and dynamic pressure distributions are not directly measurable by using conventional non-intrusive optics-based measurement techniques.

Past numerical investigations of the flow between coaxial rotating cylinders have mainly aligned with the established experimental practice of exploring the meridional plane. Baier [27] used numerical technique to predict the distribution of the velocity magnitude. Haut et al. [28], Parker and Merati [29], Deng et al. [30], Deng [31] and Deshmukh et al. [32] also performed Computational Fluid Dynamic (CFD) simulations to investigate the various flow patterns and regimes in the meridional plane.

It is surprising to note that little contributions have been reported in the literature on the pressure distribution across both the meridional and the axial planes. This offers an opportunity for exploring the annular flow beyond the confinement of the meridional plane and for making a tangible contribution to the state of the art. This paper realizes this opportunity by using three-dimensional CFD. The CFD approach provides the advantage of being able to investigate flow features across the entire annulus on the axial, the cascade, and the meridional planes. In addition, the time-average of the flow instabilities triggered due to the rotation of the inner shaft can also be resolved. Furthermore, the CFD model enables to qualify and quantify this important flow field beyond the current limitations of conventional non-intrusive optics-based measurement techniques.

This study therefore aims to examine the pressure distributions both in the meridional and in the axial planes in a concentric cylinder of a moderately wide gap set-up of a fixed outer tube and

rotating inner shaft. By combining multiple viewpoints, this paper offers a new more holistic insight into the three-dimensional pressure field between concentric cylinders, which lends itself to be understood mostly through considerations of radial momentum equilibrium. In this respect, this paper complements and completes the analysis of the flow velocity distribution across the entire annulus presented by Adebayo and Rona [33].

The CFD prediction are validated by comparing the velocity profiles from the simulations with Particle Image Velocimetry (PIV) measurements by Adebayo and Rona [23-24] in the meridional plane.

At the Taylor numbers  $2.35 \times 10^6$  and  $6.47 \times 10^6$  and at the Reynolds numbers  $1.97 \times 10^3$  and  $2.88 \times 10^3$ , the wider clearance Taylor flow is predicted to develop noticeable gauge static pressure axial variations along the fixed outer cylinder wall. These take the form of axially stacked rings of enhanced and reduced wall gauge static pressure, alternating axially. Little is reported in the literature about this feature, which is herein detailed in section 5.3. The exploitation potential of this novel insight is outlined in section 5.3, with specific reference to vertical shaft water turbines, which stand to deliver significant environmental and societal impacts from their performance enhancement.

Conclusions are drawn on the significant implications of these findings for lightly loaded journal bearings driven at high rotational speeds and for an innovative design layout for vertical pump heads.

## **2.0 Geometry and flow conditions**

**2.1. Geometry.** In this study, a three-dimensional (3-D) numerical technique is used to investigate the pattern of the flow and the distribution of pressure across the entire annulus in the meridional and axial planes of a coaxial cylinder assembly. The configuration used in this study is defined in

relation to the cylindrical coordinates shown in Fig. 1, where the  $X$ -axis of the geometrical reference system  $(r, \theta, X)$  and the axis of the coaxial shafts coincide. Two different coaxial configurations were created using the commercial CFD pre-processor ANSYS ICEM CFD 18. The computational domain specifications for these two different coaxial assemblies are provided in Table 1. Two cases are used to perform an independent investigation of the pressure distributions and of the flow configuration within the space between the concentric shafts by varying the radius and aspect ratios. The radius ratio ( $\eta = R_i R_o^{-1}$ ) and the aspect ratio ( $\Gamma = L d^{-1}$ ) investigated were  $\eta = (0.44, 0.53)$  and  $\Gamma = (7.81, 11.36)$  respectively. The clearance ratio  $d R_i^{-1}$  is 1.28 and 0.88 respectively for test cases  $\Gamma = 7.81$  and  $\Gamma = 11.36$ . The rotating speed  $\Omega$  of the inner cylinder is kept constant at 52.36 rad/s for both test cases. Testing the assembly in air at ISA ground conditions gives a Taylor number range  $2.35 \times 10^6 \leq Ta \leq 6.47 \times 10^6$  and a Reynolds number range  $1.97 \times 10^3 \leq Re \leq 2.88 \times 10^3$ .  $Re = \rho \Omega R_i d / \mu_l$  and the air viscosity  $\mu_l$  is  $1.7894 \times 10^{-5} \text{ kg m}^{-1} \text{ s}^{-1}$ .

**2.2 Boundary conditions:** To model the internal flow between the two fully enclosed independent rotating cylinders, the CFD software package, ANSYS Fluent 18 [34] is used for all the computational processes. The axis of the cylinders is horizontal and the radial extent of the computational domain is limited to 0.114 m. Before the commencement of the simulation process, zero flow conditions are invoked across the entire computational domain. Due to the cylinders laying horizontal, gravitational acceleration effects are not modelled. Appropriate initial and boundary conditions are applied across the entire domain. Specifically, a no-slip fixed adiabatic condition is applied at the fixed outer cylindrical surface at  $R_o$  and a no-slip rotating adiabatic condition is used to model the inner shaft wall. At the right and the left end-surfaces of the cylindrical assembly, no-slip boundary conditions are employed. The whole computational control volume is fully defined by these boundaries. In all the computations in this study, the inner shaft

rotation starts impulsively at a predetermined rotational velocity. This helps to adequately match the acceleration profile between the experiment [23-24] and this computation, thereby modelling the same conditions as the experiments, where the final angular velocity of the inner shaft is reached within 1 sec. [4, 15, 16].

At the beginning of the computation, the closed type system being modelled enables some flexibility in the definition of the start-up turbulence quantities. As the computation progresses, the turbulence quantities are updated by the flow solver. The turbulence quantities in the converged solution are therefore self-determined and not influenced by any computational inflow boundary, whereas in an open system the inflow boundary would affect the solution at all times. The empirical correlations for a pipe flow reported in Adebayo and Rona [33] were used to estimate initial values for the turbulence intensity, the specific turbulent kinetic energy  $k$ , and the specific turbulent kinetic energy dissipation rate  $\varepsilon$ . The flow domain for the test case  $\Gamma = 7.81$  was initialised with uniform values of 5%,  $0.0064 \text{ m}^2/\text{s}^2$ , and  $0.0189 \text{ m}^2/\text{s}^3$  respectively for turbulence intensity,  $k$  and  $\varepsilon$ . The flow domain uniform initialization levels for the specific turbulence intensity,  $k$  and  $\varepsilon$  are 6%,  $0.0093 \text{ m}^2/\text{s}^2$ , and  $0.0478 \text{ m}^2/\text{s}^3$  respectively for the test case  $\Gamma = 11.36$ . These values model a turbulent flow regime within the gap region of the two independent rotating shaft.

### **3.0 Numerical Model**

**3.1. Computational Scheme:** Isothermal, viscous, and incompressible flow conditions were assumed for the CFD simulations. This flow is governed by the incompressible conservative laws for momentum and mass, the Navier-Stokes equations [35, 36]. A finite-volume approach is used for the discretization of the governing equations and the pressure-based segregated solver by Chorin [37] is used for the numerical integration. To estimate the convection terms of the turbulence

closure model at each finite-volume face, the values of the integrand are required. A second-order upwind scheme [35, 36] is used to determine these values by interpolation from cell averaged flow.

In this study, two turbulence models were evaluated for closing the RANS equations: The Shih et al.'s [38] realizable  $k - \varepsilon$  model and the Launder et al.'s [39] Reynolds stress model (RSM). For each of the two computational geometries, the same flow conditions were tested by these turbulence models. The preliminary results reported by Adebayo and Rona [33] showed that the realizable  $k - \varepsilon$  turbulence model predicted stronger Taylor vortices compared to the other model tested. In addition to the quantitative differences between the predictions from the RSM and the realizable  $k - \varepsilon$  model, the RSM took at least 50% more computational time to process the CFD simulations for both  $\Gamma = 7.81$  and  $\Gamma = 11.36$ . Therefore, the realizable  $k - \varepsilon$  turbulence model was judged as the best choice for computing all the CFD solutions in this study, based on the result from this preliminary test. In the case of flows that involve recirculation, rotation, and separation [34], as in this present work, the realizable  $k - \varepsilon$  model is documented as providing a better improvement on the CFD results than the standard  $k - \varepsilon$  turbulence model. Furthermore, in flows involving vortices, strong streamline curvature, and rotation [34], as in the current test cases, the realizable  $k - \varepsilon$  turbulence model has also shown significant performance compared to the basic  $k - \varepsilon$  model.

**3.2. Discretization of the computational domain:** The computational domains for the two test cases were meshed using the commercial CFD mesh generator ANSYS ICEM CFD 18.0. The unstructured hexahedral mesh of intermediate mesh density (type two) used for test case  $\Gamma = 7.81$  is shown in Fig. 1. In order to assess the mesh quality for both test cases in this study, the maximum cell skewness was evaluated and found to be within the range 0.14 – 0.40. This value shows that the skewness for all the meshes used for the assessment are within the prescribed range [34]. Bi-geometric stretching was used to cluster the mesh close to the walls, for both test cases. Stretching

factors of 1.10, 1.05, and 1.02 were used respectively on three progressively finer meshes. This gave a near-wall starting cell size of approximately 0.1 mm for the test cases  $\Gamma = 7.81$  and  $\Gamma = 11.36$ .

To evaluate the sensitivity of the CFD results upon the level of the spatial discretization, a grid independence test was conducted. Three progressively finer meshes were evaluated for each test case. These meshes are labelled as type one, type two, and type three in progressive mesh size order. The same node count was used for both test cases on each mesh size. The type one mesh has  $65 \times 55 \times 129$  nodes in  $(r, \theta, X)$ . The type two and type three meshes are obtained by progressively refining each independent spatial dimension by a factor of two. This gives  $129 \times 109 \times 257$  nodes for the type two mesh and  $257 \times 217 \times 513$  nodes for the type three mesh. To establish the independence of the predictions from the level of the spatial discretization, the predictions of the total number of vortices and of the axial distribution of static pressure, radial and axial velocities were used to monitor the mesh independence of the results. The radial velocity profiles of Fig. 2 reports the CFD result at the annular mid-region of the lower channel ( $\theta = -0.5\pi$ ) in the meridional plane for the two test cases using the three different mesh types. Fig. 2 shows a good overlap among these distributions, indicating no noticeable dependence of the axial spacing of the Taylor vortices from size of the three meshes, for both test cases. This indicates that all the three levels of spatial discretization produce the same Taylor vortex pattern and that any further increase in mesh density across the computational domain is not expected to significantly change the accuracy of the predicted RANS results.

The radial profiles from Fig. 2 were used to compute the normalized difference for each flow variable between mesh types. These differences were all less than 5% and the number of the vortices for each test case was unchanged. Therefore, the computational mesh type two was chosen for generating sufficiently grid independent CFD simulations for the two test cases.

The simulations were run on the University of Leicester 5000-core High Performance Computing (HPC) cluster Alice, using 16 cores on a single compute node, by decomposing the domain with the Metis algorithm. Steady RANS flow predictions, with residuals converged to  $10^{-6}$  of their initial value, were obtained using the Semi-Implicit Method for Pressure Linked Equations (SIMPLE) [37], typically within 2000 iterations. The typical mesh two type computation required 10 Gb RAM, 14 Gb of swap space (virtual RAM), and 20 core hours to complete, on the 2.6GHz CPUs. The corresponding computational resources for a mesh three type computation are 60 Gb RAM, 58 Gb virtual RAM, and 220 core hours.

#### 4.0 Validation of the CFD results

The CFD predicted results is assessed against the reference measurements results of the in-plane velocity surveyed by PIV on the meridional plane by Adebayo and Rona [23, 24]. The profiles of radial velocity and of axial velocity obtained from the numerical computations and from experiment [23, 24], by PIV, are shown in Fig. 3 for the test case  $\Gamma = 7.81$ . The inner shaft speed  $\Omega R_i$  is used to normalize the velocity, while the inner shaft radius  $R_i$  is used for the normalization of the lengths. The axial profiles for the axial velocity were extracted and plotted at the fixed radial coordinates  $r = R_i + 0.125d$  and  $r = R_i + 0.500d$  for the radial velocity, on the meridional plane  $\theta = -0.5\pi$ . The uncertainty in the experimental measurements are calculated and represented by the Particle Image Velocimetry error bands shown by plain dashed lines (without symbols) in the velocity profiles of Fig. 3(a, b). These error bars are sized by  $\pm 1\sigma$ , where  $\sigma$  is the standard deviation from the ensemble of one hundred PIV velocity vector maps from the experiment [23, 24].

The results from the PIV experiment and the CFD simulations at  $r = R_i + 0.125d$  in Fig. 3(a) indicate an axial flow of central symmetry with respect to  $X/R_i = 5$ , the shaft mid-length, and the magnitude of the corresponding velocity minima and maxima are almost the same. Similarly, at the

radial position  $r = R_i + 0.500d$ , Fig. 3(b) shows that the radial flow is almost symmetric about  $X/R_i = 5$ . Although in Fig. 3(a, b) there are some little discrepancies between the results from the PIV and the CFD close to the right end-wall, the CFD profiles are still lay inside the PIV measurement uncertainty band. The small differences observed between the velocity profiles from the PIV and the CFD profiles in Fig. 3(a, b) near the end-walls are due to the way the experiment was set up, in which the end-wall boundaries are aligned approximately normal to the shaft axis. A similar result is reported by Adebayo and Rona [33] for the test case  $\Gamma = 11.36$ . Overall, the spatial variation of the in-plane velocities observed by PIV is substantially reproduced by the CFD simulations. This indicates that the main time-averaged flow dynamics is correctly modelled.

The spatial variation of the in-plane velocities in Fig. 3(a, b) indicate that the wavelength of the vortices agrees between experiment and computation. For  $\Gamma = 7.81$  and  $\eta = 0.44$ , the axial wavelength of the vortices is  $\lambda_x = 1.95d$ . For  $\Gamma = 11.36$  and  $\eta = 0.53$ ,  $\lambda_x = 1.9d$ . These values broadly agree with the normalized axial wavelength predicted by a small perturbation analysis by Roberts in Donnelly and Schwarz [40] for a pair of axially unconstrained ( $\Gamma \rightarrow \infty$ ) coaxial cylinders of  $\eta = 0.50$ , which is  $\lambda_x = 2.0d$ .

## 5.0 Results and discussions

**5.1. Flow pattern in the meridional plane:** The vectors of velocity extracted along the meridional plane from the CFD simulations are presented in Fig. 4(a, b) for the test cases  $\Gamma = 7.81$  and  $\Gamma = 11.36$  respectively. In these figures, the inner cylinder surface speed  $\Omega R_i$  has been used to normalise the velocity vectors. Fig. 4(a, b) show pairs of counter-rotating axisymmetric vortices for the two test cases. This axisymmetric pattern recurs along the axial cylinder length of the whole CFD simulation domain with successive cells of the vortices driving the flow in a similar radial path at their conference points. Along the axial path of the CFD domain, which is  $10R_i$  long, four pairs of vortices

are predicted for the test case  $\Gamma = 7.81$ , while six pairs of vortices are predicted for the test case  $\Gamma = 11.36$ .

These vortices are symmetrical about the axial plane  $X/R_i = 5$  located mid-way along the axial direction. Consequently, to illustrate the flow pattern more clearly, only the vortices to the left of this plane of symmetry are shown in Fig. 4. The increase in the number of vortices from four pairs in the test case  $\Gamma = 7.81$  to six pairs in the test case  $\Gamma = 11.36$  is one of the effects of the change in the gap width  $d$ . This is an indication that the development of vortices and their number are determined by the aspect and radius ratios, in agreement with past numerical and experimental investigations by Adebayo and Rona [23, 24, 33], where the physics of the fluid motion have been analysed in more detail. This includes a discussion on the inter-vortex mixing that occurs in the radial inflow and radial outflow regions in Fig. 4. Radial outflow regions, such as at location (C) in Fig. 4, occur between two counter-rotating vortices, where fluid rotary motion with high tangential momentum close to the inner shaft is convected outwards, towards the outer cylinder. Radial inflow regions occur between adjacent counter-rotating vortex pairs, such as at location (E) in Fig. 4, and feature the transport of low tangential momentum fluid motion from the outer tube towards the inner shaft.

**5.2. Flow pattern in the axial plane:** The flow along the axial plane was analyzed in this study to complement the PIV results obtained in the meridional plane reported by Adebayo and Rona [23, 24] and provides key support for understanding the distribution of pressure in the annular space within the two independent rotating shafts as the gap width changes. Fig. 5(a-f) shows normalized velocity vector maps on various axial planes for the test cases  $\Gamma = 7.81$  and  $\Gamma = 11.36$ . Only the in-plane velocity component is reported in Fig. 5(a-f). Within the computational domain, six various flow patterns are identified. These include the flow pattern at the right and left end-walls. Out of

the six different patterns, four are repeated along the shaft axis with a spatial pitch of one Taylor vortex pair. In Fig. 4, the axial locations of these various patterns are labelled alphabetically (A-E) for easy identification. The axial location of pattern F, which is not shown in Fig. 4, is close to the right end-wall at  $X/R_i = 9.95$ . The axial locations of the remaining patterns are: (A)  $X/R_i = 0.05$ , (B)  $X/R_i = 0.92$ , and (C)  $X/R_i = 1.47$ , in Fig. 4(a), and (D)  $X/R_i = 1.41$  and (E)  $X/R_i = 1.84$ , in Fig. 4(b).

The velocity vector maps at  $X/R_i = 1.97$ ,  $X/R_i = 2.62$ , and  $X/R_i = 9.95$  for the test case  $\Gamma = 7.81$ , reported in Adebayo and Rona [33], give similar patterns as the velocity vector maps in Fig. 5(d-f) for the test case  $\Gamma = 11.36$ . Likewise, velocity vector maps at  $X/R_i = 0.05$ ,  $X/R_i = 0.65$ , and  $X/R_i = 1.07$  for  $\Gamma = 11.36$ , also reported in Adebayo and Rona [33], are similar to the velocity vector maps in Fig. 5(a-c) for test case  $\Gamma = 7.81$ . On each velocity map in Fig. 5, the reference vector is shown. This helps to appreciate the scale of the vectors. The flow features on each axial plane are discussed in greater detail in Adebayo and Rona [33].

**5.3. Pressure distribution across the meridional plane:** The distribution of pressure in the gap between coaxial shafts is an essential feature in the design of bearing chambers, pumps, and of journal bearings. The distribution of the pressure is as result of the equilibrium between the centrifugal force and the radial pressure gradient that are related with the rotary motion, such that  $\partial p / \partial r = \rho \omega^2 r$ .

Furthermore, the distribution of pressure is important for the development of vortex cells and for the staging among various Taylor-Couette flow patterns and regimes in the gap between independent rotating cylinders [31]. In both the test cases  $\Gamma = 7.81$  and  $\Gamma = 11.36$  discussed in this study, the pressure distributions have been normalized by  $0.5\rho R_i^2 \Omega^2$ .

Axial profiles of pressure at three constant radial positions in the upper ( $\theta = 0.5\pi$ ) and lower ( $\theta = -0.5\pi$ ) sections of the meridional plane have been extracted and plotted to detail the spatial

variation of the pressure distribution in the meridional plane. The radial coordinates from which the three extractions are obtained for  $\Gamma = 11.36$  are: (i)  $r = R_i + 0.045d$ , which is 1 mm distant from the surface of the inner shaft; (ii)  $r = R_i + 0.500d$ , which is the gap mid-span between the two cylinders, and (iii)  $r = R_i + 0.955d$ , which is 1 mm distant from the surface of the stationary outer tube. For  $\Gamma = 7.81$ , the locations of the radial line along which the results are extracted are at the same fraction of gap width  $d$  as for  $\Gamma = 11.36$ .

The gauge static pressure (GSP) results in the meridional plane for  $\Gamma = 7.81$  and  $\Gamma = 11.36$  are presented in Fig. 6(a, b). The spatial distributions of GSP at the same radial distance in these figures do not depend on the sign of the angle  $\theta$  on the  $\theta = \pm 0.5\pi$  meridional plane. A positive radial pressure gradient is displayed by the profiles, by which the GSP near to the wall of the fixed outer tube at position  $r = R_i + 0.955d$  (denoted by the red lines with squares) is greater than the GSP close to the surface of the rotating inner shaft at position  $r = R_i + 0.045d$ . This results from the flow radial momentum equilibrium generated by its tangential velocity distribution. Specifically, the rotating inner shaft creates a  $\tau_{r\theta}$  shear stress which acts on the fluid particles away from the wall. These particles are set in motion tangent to their instantaneous radial position. The outer cylinder provides radial confinement to the motion of these particles, inducing them to rotate about the cylinder axis. A radial pressure gradient provides the centripetal acceleration required for keeping the fluid particles on a circular path. This justifies the increase in GSP close to the surface of the fixed outer tube and the decrement in GSP near to the wall of the rotating inner shaft shown in Fig. 6. This scenario is similar to that in which fluid particles in a single-stage centrifugal pump are expelled from the tips of the impeller vanes at high velocity. Then, their motion is radially confined by the volute, which decelerates the flow and converts its kinetic energy into flow energy (pressure rise). Fig. 6(a) and Fig. 6(b) are suggestive of a similar energy conversion process taking place between

the coaxial rotating cylinders, as evidenced by the radial pressure gradient in the form of an increase in the radial pressure from the rotating inner shaft to the stationary outer tube.

Close to the surface of the rotating inner shaft at position  $r = R_i + 0.045d$  in Fig. 6(a, b), negative GSP minima (troughs) are present in the outward flow regions and GSP maxima (peaks) occur in the inward flow regions of Fig. 4(a, b). The GSP peaks are shown to be sharper compared to the negative GSP troughs at this radial position. This feature can be credited to the impingement of the radial inflow against the rotating inner shaft surface, which determines a more localized stagnation region with respect to the radial outflow moving away from this surface.

In Fig. 6(a) and Fig. 6(b), near to the surface of the outer tube, at position  $r = R_i + 0.955d$ , GSP maxima can be observed instead in the outward flow regions and a lower GSP is observed in the inward flow regions of Fig. 4(a) and Fig. 4(b). At the outward flow regions, the GSP peaks are observed to be sharper at this radial position, whereas at the inward flow regions, the GSP troughs are observed to be flatter. This feature can be attributed to the more localized stagnation region that the radial outflow forms by impinging against the outer cylinder wall with respect to the inflow that moves away from this surface. Fig. 6(a) and Fig. 6(b) show that there is a noticeable change in the difference in static pressure between the fixed outer tubes and rotating inner shaft surfaces with axial position. The outward flow regions display the largest difference and the inward flow regions display the smallest difference. This feature is explained in section 5.4, by considering the flow radial momentum equilibrium in a Taylor vortex cell.

Knowledge of the static pressure spatial distribution in the annular space between a coaxial rotating inner shaft and a fixed outer tube is considered useful in the design of a vertical turbine pump head. It is important that the pump designers design pumps such that the maximum gauge static pressure location is aligned with the central axis of the delivery pipe of the pump in order to attain maximum head delivery, thereby resulting in a higher pump mechanical efficiency.

The profiles of the normalized dynamic pressure at positions  $r = R_i + 0.045d$ ,  $r = R_i + 0.500d$ , and  $r = R_i + 0.955d$  for  $\Gamma = 11.36$  and  $\Gamma = 7.81$  are presented respectively in Fig. 7(a) and in Fig. 7(b). From these profiles, the dynamic pressure near to the rotating inner wall surface is observed to be high. This decreases progressively toward the fixed outer tube surface. This observation is not unexpected, as the fluid particles close to the stationary outer tube have a lower tangential momentum compared to the fluid particles close to the rotating inner shaft. The effect is a low dynamic pressure near the wall of the stationary outer tube and a high dynamic pressure near the wall of the rotating inner shaft. Consider now the normalized dynamic pressure profiles near to the inner shaft surface presented in Fig. 7(a) and Fig. 7(b). In these profiles, dynamic pressure maxima exist in the outward flow regions of Fig. 4(a, b), while dynamic pressure minima are present in the inward flow regions of Fig. 4(a, b). In the outward flow regions, the shape of the dynamic pressure maxima (peaks) is shaper compared to the shape of the dynamic pressure minima (troughs). This pattern is caused by the inner cylinder imparting a tangential acceleration through surface shear stress to the inward flow that approaches this rotating surface with a lower tangential momentum. As the accelerated fluid particles flow outwards, they conserve their acquired tangential momentum as they funnel outwards between adjacent vortex pairs.

At position  $r = R_i + 0.500d$ , the trough of dynamic pressure is almost flat and not well-defined at the inward flow regions of Fig. 4(a) and Fig. 4(b). This pattern can be associated to the difference in vortex induced velocity in the meridional plane, since the centers of the vortices are further apart from the inflow axial planes (E) than from the outflow axial planes (C). This results in the reduction of the strength of the vortex induced velocity, which explains the flattening of the local dynamic pressure profile. At radial position  $r = R_i + 0.500d$ , the fluid tangential momentum is lower compared to the tangential momentum of fluid near to the surface of the rotating inner shaft. This explains the discrepancies between the dynamic pressure at position  $r = R_i + 0.045d$  and the

dynamic pressure at position  $r = R_i + 0.500d$ , with the former being higher than the latter. In the same manner, the dynamic pressure at positions  $r = R_i + 0.500d$  and  $r = R_i + 0.045d$  is higher compared to the dynamic pressure close to the surface of the stationary outer tube at position  $r = R_i + 0.955d$ . This is because the fluid particles close to the stationary outer tube wall have a lower tangential momentum.

**5.4. Pressure distribution in the axial plane:** In Adebayo and Rona [33], the azimuthal distribution of the tangential velocity in the axial planes  $X/R_i = 2.62$  and  $X/R_i = 1.07$  for the test cases  $\Gamma = 7.81$  and  $\Gamma = 11.36$  were indicative of an axisymmetric flow. This is further substantiated in this paper, by examining the azimuthal distribution of the dynamic pressure at the constant radial positions  $(r - R_i)d^{-1}$  of 0.045, 0.500, and 0.955.

Fig. 8(a) shows the numerical results in the axial plane  $X/R_i = 2.62$  for the test case  $\Gamma = 7.81$ . At all the three radial positions, the dynamic pressure is essentially constant and nearly independent from the azimuthal coordinate  $\theta$ . The insert in Fig. 8(a) is a magnification of the plot area close to the origin that shows this feature more clearly. For the test case  $\Gamma = 11.36$ , along the axial plane  $X/R_i = 1.07$ , similar results are presented in Fig. 8(b). This indicates that the flow does not manifest any appreciable waviness of the Taylor vortices.

The radial pressure distributions at the axial locations (B) to (E) of Fig. 4 were extracted for the test cases  $\Gamma = 7.81$  and  $\Gamma = 11.36$  similarly to the radial velocity profiles extracted in Adebayo and Rona [33]. The results are shown in Fig. 9 (a) and (b). Near to the wall of the rotating inner shaft, these profiles show that the normalized gauge static pressure (GSP) is lowest, while it is highest near to the surface of the fixed outer tube. This result confirms the trend highlighted in Fig. 6 about the radial pressure distribution being driven by the radial momentum equilibrium in the rotating flow, by which  $\partial p/\partial r = \rho\omega^2 r$ . This results in the GSP at the fixed outer tube surface being greater compared to the GSP at the rotating inner shaft surface.

Close to the left and right end boundaries at positions  $X/R_i = 0.05$  and  $X/R_i = 9.95$ , the normalized gauge static pressure profiles substantially overlap. On these axial planes, the normalized gauge static pressure distributions presented in Fig. 9 display a lower radial gradient with increasing  $r$  for both  $\Gamma = 7.81$  and  $\Gamma = 11.36$  compared to the pressure distributions on other axial planes. The lower radial gradient with increasing  $r$ , in these results, may be due to some of the centrifugal forces in the flow being counter-balanced by the viscous forces in the regions adjacent to the two end-walls. The implication is a reduction in the radial pressure gradient, as predicted.

The results of normalized GSP along the axial plane extracted through the center of the clockwise ( $X/R_i = 0.92$ ) and of the anti-clockwise ( $X/R_i = 1.97$ ) vortices, in Fig. 9(a), show that the Taylor vortices exhibit similar trends to one another with the profiles substantially overlapping each other. Fig. 9(b) for the test case  $\Gamma = 11.36$  shows Taylor vortices with similar trends as in Fig. 9(a).

The radial profiles of normalized GSP in the outflow regions, at  $X/R_i = 1.47$  for  $\Gamma = 7.81$  and at  $X/R_i = 1.07$  for  $\Gamma = 11.36$ , are shown respectively in Fig. 9(a) and Fig. 9(b). At the surface of the stationary outer cylinder, in the outflow regions, the normalized gauge static pressure is observed to have a higher value than that on any other axial plane in the entire computational domain.

Fig. 9(a) and Fig. 9(b) show respectively the results of normalized GSP in the inward flow regions at positions  $X/R_i = 2.62$  for the test case  $\Gamma = 7.81$  and  $X/R_i = 1.84$  for the test case  $\Gamma = 11.36$ . Near the outer tube, the value of the normalized GSP is similar to that at the same radial location in the axial plane through a vortex center. The normalized gauge static pressure at this location is small compared to the normalized GSP maximum in the outflow region as the flow loses tangential momentum by friction against the outer cylinder wall as it travels from the outflow to the inflow region along this wall. This reduces the pressure required for radial momentum equilibrium. The particles of this flow with a reduced tangential momentum are then drawn inwards, in an inflow

region. Their reduced angular velocity gives the shallower normalized gauge static pressure gradient shown in Fig. 9(a) and Fig. 9(b), by radial equilibrium.

Fig. 10(a) and Fig. 10(b) display the normalized dynamic pressure at the same positions as in Fig. 9(a) and Fig. 9(b) for  $\Gamma = 7.81$  and  $\Gamma = 11.36$ . Fig. 10(a) and Fig. 10(b) exhibit a similar trend for all the profiles with the normalized dynamic pressure at its maximum near to the wall of the rotating inner shaft and then progressively decreasing toward the fixed outer tube. This trend lends itself to a simple explanation. The tangential flow motion is driven by the rotating inner shaft, resulting in maximum tangential momentum. This is the dominant contributor to the dynamic pressure at the surface of the inner shaft. As indicated in Fig. 5, the flow tangential velocity slowly reduces toward the fixed outer tube surface. This is shown more clearly in the radial profiles of tangential velocity reported in Adebayo and Rona [33]. This reduction of the fluid velocity results in a corresponding decrease in the dynamic pressure, since the dynamic pressure is proportional to the square of the fluid velocity. The value of the dynamic pressure at the fixed outer tube is approximately equal to zero, due to the no-slip condition used at this boundary.

Close to the left end-wall at  $X/R_i = 0.05$  and close to the right end-wall at  $X/R_i = 9.95$ , the normalized dynamic pressure profiles shown in Fig. 10(a) for the test case  $\Gamma = 7.81$  exhibit similar trends to one another with the profiles substantially overlapping. The normalized dynamic pressure is observed to be smaller than further away from the end walls, as a result of the viscous effects at the boundary layer of the left and right end-walls that reduce the near-wall velocity magnitude.

The normalized dynamic pressure at  $X/R_i = 0.05$  and at  $X/R_i = 9.95$  and through the vortex centers at  $X/R_i = 0.92$  and at  $X/R_i = 1.97$  all show three regions where the profiles change. Near the surface of the rotating inner shaft, the normalized dynamic pressure decreases rapidly with increasing radial distance. In the middle region of the annulus, the normalized dynamic pressure plateaus. The normalized dynamic pressure then further reduces toward the surface of the fixed

outer tube. At the wall of the fixed outer tube, on which a no-slip condition is applied, the dynamic pressure reduces to approximately zero. The normalized dynamic pressure profiles in Fig. 10(b) for the test case  $\Gamma = 11.36$  exhibit similar trends as in Fig. 10(a).

Across the axial planes of outflow  $X/R_i = 1.47$  for the test case  $\Gamma = 7.81$  in Fig. 10(a) and  $X/R_i = 1.07$  for the test case  $\Gamma = 11.36$  in Fig. 10(b), the radial profiles of normalized dynamic pressure exhibit a different pattern when compared with the other profiles at different radial positions in Fig. 10(a) and Fig. 10(b). A similar overall pattern is shown, from the surface of the inner shaft, where the normalized dynamic pressure diminishes and reaches the value of zero at the surface of the fixed outer tube. However, in Fig. 10(a) and in Fig. 10(b), it is observed that the normalized dynamic pressure curve in the outflow region is above all the other curves. This is due to the outward flow region transporting flow particles with high tangential momentum radially between two adjacent vortices.

Across the axial planes through inward flow regions,  $X/R_i = 2.62$  for the test case  $\Gamma = 7.81$  in Fig. 10(a) and  $X/R_i = 1.84$  for the test case  $\Gamma = 11.36$  in Fig. 10(b), it is observed that the radial profiles of normalized dynamic pressure decreases non-uniformly, with the dynamic pressure exhibiting different gradients. The rate at which the fluid from the two adjacent vortices is mixing at their meeting point varies because the outward flow region convects high momentum fluid and inward flow region convects low momentum fluid, resulting in the change in the dynamic pressure trends through the outflow and inflow regions observed in these positions.

## Conclusions

In this paper, the flow between two independent concentric rotating shafts of  $\eta = 0.44$  and  $\eta = 0.53$ ,  $\Gamma = 7.81$  and  $\Gamma = 11.36$ ,  $\mu = 0$ , and  $Ta = 6.47 \times 10^6$  and  $2.35 \times 10^6$  has been modelled by Computational Fluid Dynamics. Whereas many of the previous studies that investigated the Taylor vortex flow

concentrated on the analysis of the velocity distributions in the meridional plane, this current study documents qualitative and quantitative predictions of the spatial distribution of static and of dynamic pressure on the meridional and on the axial planes across the entire annulus, which have not been previously reported.

The static and dynamics pressures exhibit non-uniform distributions axially and radially, whereas pressure was found to be substantially uniform in the azimuthal direction, indicating an axisymmetric Taylor vortex flow. It was found that most of the predicted axial and radial pressure changes in the rotating flow could be explained by the principle of radial momentum equilibrium, by considering the spatial distribution of the flow tangential velocity generated by the Taylor vortices. This seems to be the main driver of the Taylor vortex flow static pressure distribution at the selected test conditions.

The surface of the stationary outer cylinder is shown to contain regularly spaced gauge static pressure maxima that follow the axial stacking of steady Taylor vortices. The dynamic pressure of the annular flow near to the fixed outer tube is also highest in the neighborhood of these maxima, which are outflow regions of the Taylor vortex flow.

This insight has a good potential for practical engineering applications. Lightly loaded journal bearings operated at high angular speeds may develop the observed pressure pattern, which would result in rings of greater pressure on the casing that may lead to a reduced bearing life span.

In a vertical turbine pump, the observed flow behavior may be used for improving the hydro-mechanical performance of the pump. These devices are commonly used for the irrigation of crops. By suitably locating the pump outlet on the up-riser pipe, this can match the axial location of a gauge static pressure maximum determined by the Taylor vortex flow. This would add to the pressure rise produced by the submerged impeller and could increase the hydro-mechanical efficiency of the pump.

Where the objective of the pumping action is the effective displacement of fluid as opposed to its pressure rise, it may be appropriate to locate the pump outlet at a position of maximum dynamic pressure, in the axial planes of outflow between Taylor vortices, to exploit the radially outwards flow motion. Further research is required to substantiate and verify this approach.

### **Acknowledgment**

The authors would like to acknowledge the support by the European Community's Sixth Framework Programme (PROVAEN, project number 32669). The licenses for the software used for processing and plotting the graphical data were acquired with the support of EPSRC on grant GR/N23745/01. This research used the ALICE High Performance Computing Facility at the University of Leicester.

### **Funding**

- [1] The European Commission (EC)
- [2] The Research Council UK (RCUK)

**Nomenclature**

$\eta = R_i/R_o$	The radius ratio
$d = R_o - R_i$	The gap-width, m
$\Omega$	The rotational speed of the inner shaft, rad/s
$\nu$	The fluid kinematic viscosity, m <sup>2</sup> /s
$R_i$	the inner shaft radius, m
$R_o$	the outer tube radius, m
Ta	Taylor number
Re	Reynolds number
$r, \theta, X$	Cylindrical reference system, m and rad
$\Gamma = Ld^{-1}$	The aspect ratio
$L$	The length of the cylinders in the axial direction
$k$	Specific turbulent kinetic energy, m <sup>2</sup> /s <sup>2</sup>
$\varepsilon$	Specific turbulent kinetic energy dissipation rate, m <sup>2</sup> /s <sup>3</sup>
$\omega$	The flow angular velocity, rad/s
$\rho$	Fluid density, kg/m <sup>3</sup>
$\sigma$	The standard deviation
$\mu$	Outer to inner cylinder rotational speed ratio
$\mu_l$	Molecular viscosity, kg m <sup>-1</sup> s <sup>-1</sup>
$\lambda_x$	Axial wavelength of the Taylor vortices, m

## References

- [1] Mallock, A., 1888, "Determination of the viscosity of water," *Proceedings of the Royal Society of London*, **45**, 126-132.
- [2] Mallock, A., 1896, "Experiments on fluid viscosity," *Philosophical Transactions of the Royal Society of London Series A*, **187**, 41-56.
- [3] Taylor, G. I., 1923, "Stability of a viscous liquid contained between two rotating cylinders," *Philosophical Transactions of the Royal Society of London Series A*, **223**, 289-343.
- [4] Chandrasekhar, S., 1958, "The stability of viscous flow between rotating cylinders," *Proceedings of the Royal Society of London Series A*, **246** (1246), 301-311.
- [5] Davis, M. W., and Weber, E. J., 1960, "Liquid-liquid extraction between rotating concentric cylinders," *Industrial and Engineering Chemistry Research*, **52** (11), 929-934.
- [6] Bernstein, G. J., Grodsvenor, D. E., Lenc, J. F., and Levitz, N. M., 1973, "Development and performance of a high-speed annular centrifugal contactor," Report No. ANL-7968, Argonne National Laboratory, Argonne, IL.
- [7] Ogihara, T., Matsuda, G., Yanagawa, T., Ogata, N., and Fujita, N. M., 1995, "Continuous synthesis of monodispersed silica particles using Couette-Taylor vortex flow," *Journal of the Ceramic Society of Japan*, **103** (1194), 151-154.
- [8] Imamura, T., Saito, K., Ishikura, S., and Nomura, M., 1993, "A new approach to continuous emulsion polymerization," *Polymer International*, **30**, 203-206.
- [9] Tsao, Y. M. D., Boyd, E., and Spaulding, G., 1994, "Fluid dynamics within a rotating bioreactor in space and earth environments," *Journal of Spacecraft and Rockets*, **31** (6), 937- 943.
- [10] Sczechowski, J. G., Koval, C. A., and Noble, R. D., 1995, "A Taylor vortex reactor for heterogeneous photocatalysis," *Chemical Engineering Science*, **50**, 3163-3173.
- [11] Nicholas, A., 2009, "Reducing electrical energy consumption by five percent," Grundfos Holding A/S, Denmark.
- [12] International Energy Agency, 2015, "Key world energy statistics," Chirat press, France.
- [13] Couette, M., 1890, "Études sur le frottement des liquids," *Ann. Chim. Phys*, **6**, 433-510.
- [14] Jeffreys, H., 1928, "Some cases of instability in fluid motion," *Proceedings of the Royal Society of London Series A*, **118**, 195-208.
- [15] Chandrasekhar, S., 1961, "Hydrodynamic and hydromagnetic stability," First edition, Oxford University press, Oxford.
- [16] Di Prima, R. C., 1961, "Stability of non-rotationally symmetric disturbances for viscous flow

between rotating cylinders,” *Physics of Fluids*, **20**, 751-755.

- [17] Andereck, C. D., Liu, S. S., and Swinney, H. L., 1986, “Flow regimes in a circular Couette system with independently rotating cylinders,” *Journal of Fluid Mechanics*, **164**, 155-183.
- [18] Coles, D., 1965, “Transition in circular Couette flow,” *Journal of Fluid Mechanics*, **21**, 385-425.
- [19] Koschmieder, E. L., 1979, “Turbulent Taylor vortex flow,” *Journal of Fluid Mechanics*, **93**, 515-527.
- [20] Liao, C. B., Jane, S. J., and Young, D. L., 1999, “Numerical simulation of three-dimensional Couette-Taylor flows,” *International Journal for Numerical Methods in Fluids*, **29**, 827-847.
- [21] Czarny, O., Serre, E., Bontoux, P., and Lueptow, R. M., 2002, “Spiral and wavy vortex flows in short counter-rotating Taylor-Couette cells,” *Theoretical and Computational Fluid Dynamics*, **16** (1), 5-15.
- [22] Serre, E., Crespo del Arco, E., and Bontoux, P., 2001, “Annular and spiral patterns in flows between rotating and stationary discs,” *Journal of Fluid Mechanics*, **434**, 65-100.
- [23] Adebayo, D., and Rona, A., 2015, “The persistence of vortex structures between rotating cylinders in the  $10^6$  Taylor number range,” *International Review of Aerospace Engineering (I.RE.AS.E)*, **8** (1), 16-25.
- [24] Adebayo, D., and Rona, A., 2015, “PIV study of the flow across the meridional plane of rotating cylinders with wide gap,” *International Review of Aerospace Engineering (I.RE.AS.E)*, **8** (1), 26-34.
- [25] Wereley, S. T., and Lueptow, R. M., 1994, “Azimuthal velocity in supercritical circular Couette flow,” *Experiments in Fluids*, **18**, 1-9.
- [26] Wereley, S. T., and Lueptow, R. M., 1998, “Spatio-temporal character of non-wavy and wavy Taylor-Couette flow,” *Journal of Fluid Mechanics*, **364**, 59-80.
- [27] Baier, G., 1999, “Liquid-liquid extraction based on a new flow pattern: Two-fluid Taylor-Couette flow,” PhD thesis, University of Wisconsin, USA.
- [28] Haut, B., Amor, H. B., Coulon, L., Jacquet, A., and Halloin, V., 2003, “Hydrodynamics and mass transfer in a Couette-Taylor bioreactor for the culture of animal cells,” *Chemical Engineering Science*, **58**, 774 -784.
- [29] Parker, J., and Merati, P., 1996, “An investigation of turbulent Taylor-Couette flow using Laser Doppler Velocimetry in a refractive index matched facility,” *Journal of Fluids Engineering*, **118** (4), 810-818.
- [30] Deng, R., Arifin, D. Y., Mak, Y. C., and Wang, C., 2009, “Characterisation of Taylor vortex flow in a short liquid column,” *Journal of American Institute of Chemical Engineers*, **55** (12),

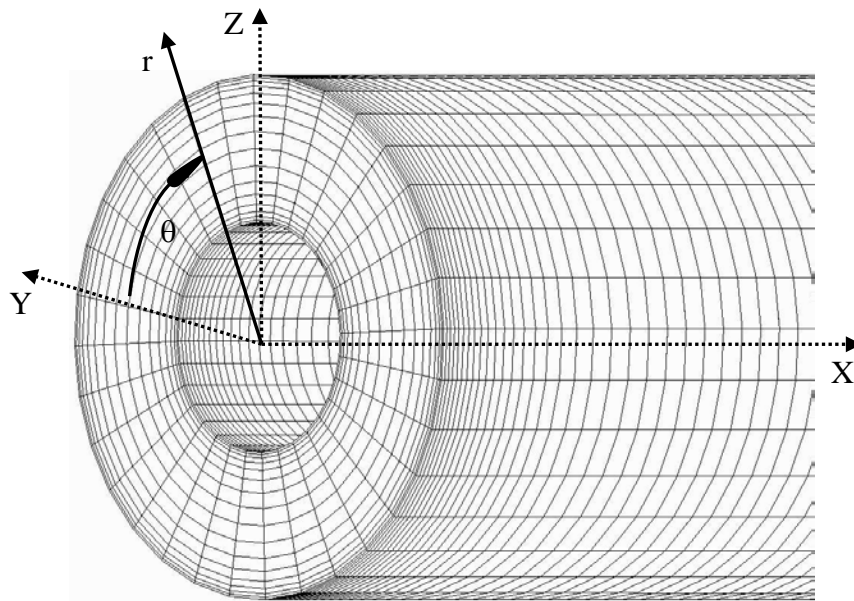
3056 -3065.

- [31] Deng, D., 2007, "A numerical and experimental investigation of Taylor flow instabilities in narrow gaps and their relationship to turbulent flow in bearings," PhD thesis, The University of Akron, USA.
- [32] Deshmukh, S. S., Vedantam, S., Joshi, J. B., and Koganti, S. B., 2007, "Computational flow modeling and visualization in the annular region of annular centrifugal extractor," *Industrial and Engineering Chemistry Research*, **46** (25), 8343-8354.
- [33] Adebayo, D., and Rona, A., 2016), "The three-dimensional velocity distribution of wide gap Taylor-Couette flow modelled by CFD," *International Journal of Rotating Machinery*, Vol. **2016**, Article ID 8584067, 1-11.
- [34] ANSYS FLUENT, 2009, "Fluent 12.0 User's Manual Guide," Fluent Incorporated, Lebanon, NH, USA.
- [35] Versteeg, H. K., and Malalasekera, W., 1995, "An introduction to computational fluid dynamics: the finite volume method," Essex, UK, Pearson Prentice Hall.
- [36] Anderson, J. D., 1995, "Computational fluid dynamics: the basics with applications," New York, McGraw-Hill.
- [37] Chorin, A. J., 1968, "Numerical solution of the Navier-Stokes equations," *Mathematics of Computation*, **22**, 745-762, 1968.
- [38] Shih, T.-H., Liou, W. W., Shabbir, A., Yang, Z., and Zhu, J., 1995, "A new k-epsilon eddy-viscosity model for high Reynolds number turbulent flows - Model development and validation," *Computers & Fluids*, **24** (3), 227-238.
- [39] Launder, B. E., Reece, G. J., and Rodi, W., 1975, "Progress in the development of a Reynolds-stress turbulence closure," *Journal of Fluid Mechanics*, **68** (3), 537-566.
- [40] Donnelly, R. J., and Schwarz, K. W., 1965, "Experiments on the stability of viscous flow between rotating cylinders. VI. Finite-amplitude experiments," *Proceedings of the Royal Society of London Series A*, **283**, 531-556.

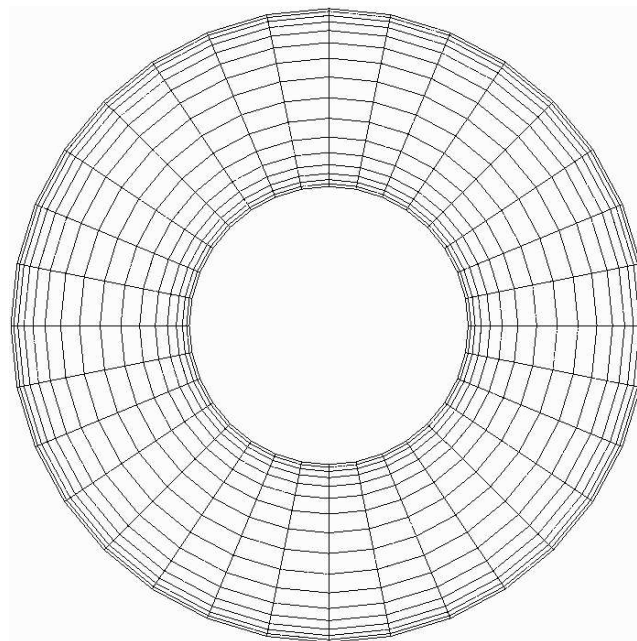
### Figure Captions List

- Fig. 1 (a) Hexahedral computational mesh structure and (b) computational mesh detail at the end wall. One mesh point every two in  $X$ ,  $r$ , and  $\theta$  has been plotted for clarity.
- Fig. 2 Radial velocity profiles at  $r = R_i + 0.500d$  for three different levels of computational mesh refinement for test cases (a)  $\Gamma = 7.81$  and (b)  $\Gamma = 11.36$ . ( $\diamond$ ) Mesh type 1, ( $\square$ ) mesh type 2, and ( $\triangleright$ ) mesh type 3.
- Fig. 3 Normalized (a) axial and (b) radial velocity profiles from PIV and CFD at the constant radial positions  $r = R_i + 0.125d$  and  $r = R_i + 0.500d$  on the meridional plane at  $\theta = -0.5\pi$ , with the PIV error band.  $\Gamma = 7.81$ .
- Fig. 4 Normalized velocity vectors in the meridional plane of the annulus for test cases (a)  $\Gamma = 7.81$  and (b)  $\Gamma = 11.36$ . The reference velocity vector is  $0.5\Omega R_i$ .
- Fig. 5 Velocity vectors on different axial planes normalized by  $\Omega R_i$ .
- Fig. 6 Normalized gauge static pressure profiles in the meridional plane at constant radial positions, ( $\triangleright$ )  $r = R_i + 0.045d$ , ( $\diamond$ )  $r = R_i + 0.500d$ , and ( $\square$ )  $r = R_i + 0.955d$  for the test cases (a)  $\Gamma = 7.81$  and (b)  $\Gamma = 11.36$ . (—)  $\theta = 0.5\pi$ , (--)  $\theta = -0.5\pi$ .
- Fig. 7 Normalized dynamic pressure profiles in the meridional plane at constant radial positions ( $\triangleright$ )  $r = R_i + 0.045d$ , ( $\diamond$ )  $r = R_i + 0.500d$ , and ( $\square$ )  $r = R_i + 0.955d$  for the test cases (a)  $\Gamma = 7.81$  and (b)  $\Gamma = 11.36$ . (—)  $\theta = 0.5\pi$ , (--)  $\theta = -0.5\pi$ .
- Fig. 8 Azimuthal profiles of normalized dynamic pressure at different radii on selected axial planes for the test cases (a)  $\Gamma = 7.81$  and (b)  $\Gamma = 11.36$ . ( $\triangleright$ )  $r = R_i + 0.045d$ , ( $\diamond$ )  $r = R_i + 0.500d$ , and ( $\square$ )  $r = R_i + 0.955d$ .
- Fig. 9 Normalized gauge static pressure profiles on different axial planes at  $\theta = -0.5\pi$ , (a)  $\Gamma = 7.81$  and (b)  $\Gamma = 11.36$ .

Fig. 10 Normalized dynamic pressure profiles on different axial planes at  $\theta = -0.5\pi$ , (a)  $\Gamma = 7.81$  and (b)  $\Gamma = 11.36$ .

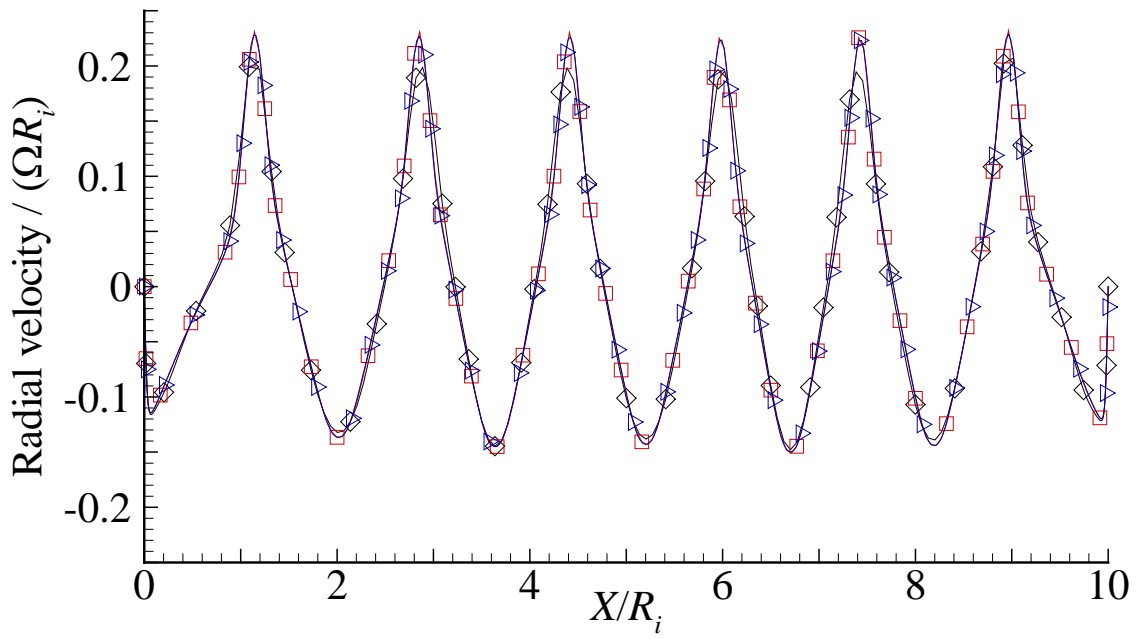


(a)

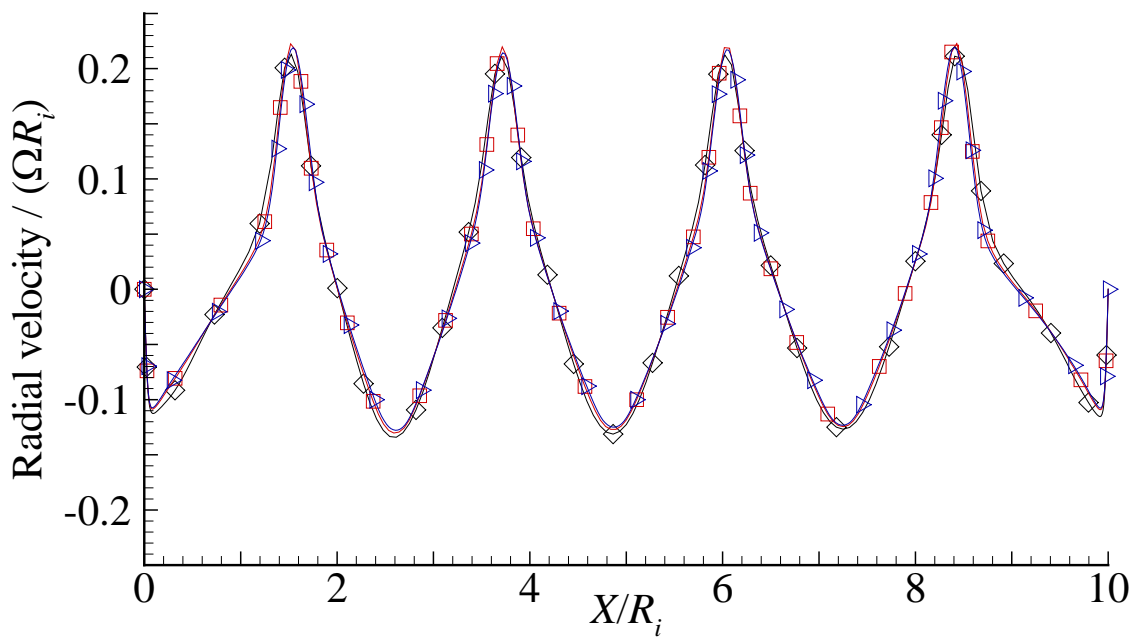


(b)

Fig. 1. (a) Hexahedral computational mesh structure and (b) computational mesh detail at the end wall. One mesh point every two in  $X$ ,  $r$ , and  $\theta$  has been plotted for clarity.



(a)



(b)

Fig. 2. Radial velocity profiles at  $r = R_i + 0.500d$  for three different levels of computational mesh refinement for test cases (a)  $\Gamma = 7.81$  and (b)  $\Gamma = 11.36$ . ( $\diamond$ ) Mesh type 1, ( $\square$ ) mesh type 2, and ( $\triangleright$ ) mesh type 3.

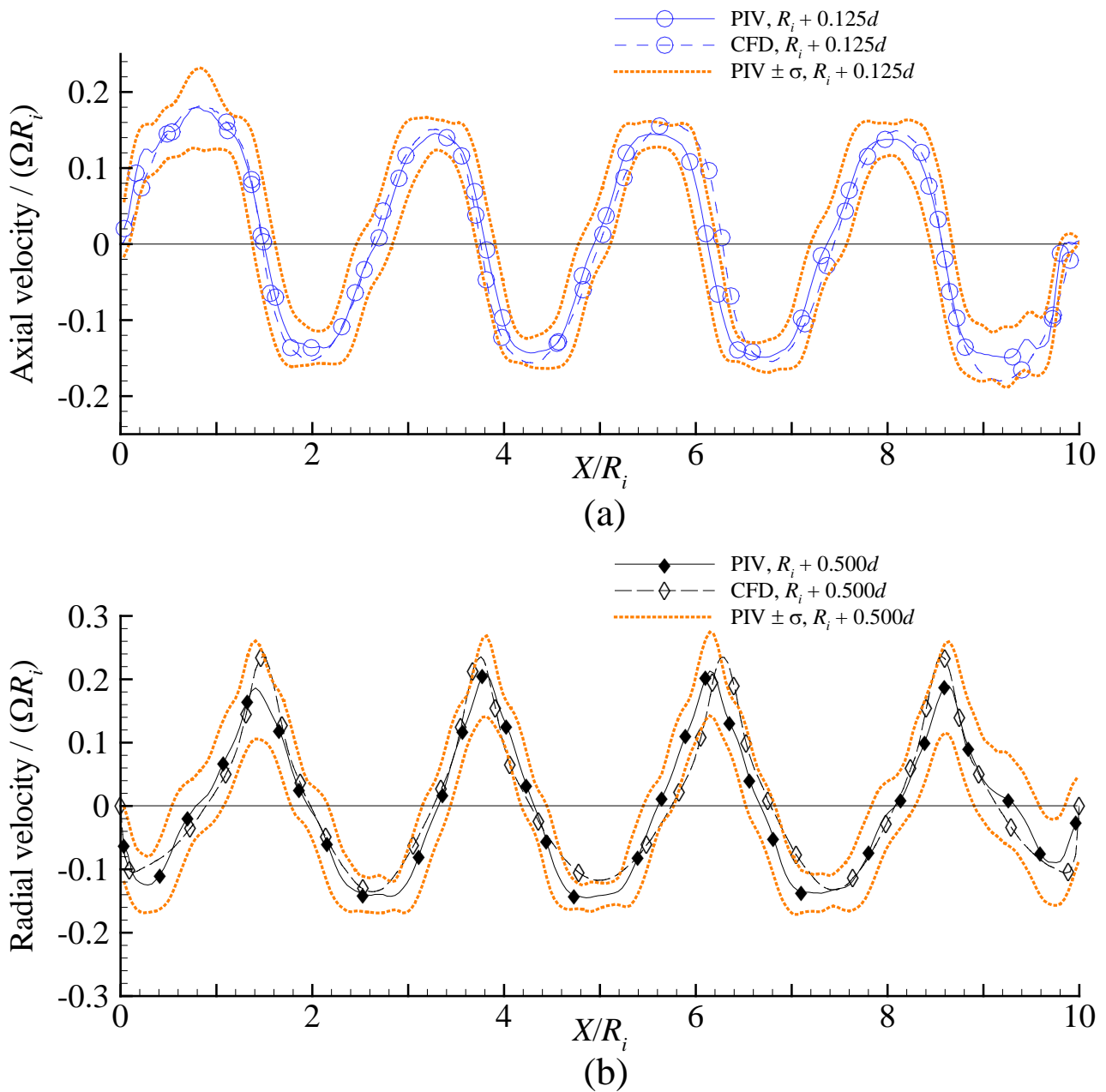


Fig. 3. Normalized (a) axial and (b) radial velocity profiles from PIV and CFD at the constant radial positions  $r = R_i + 0.125d$  and  $r = R_i + 0.500d$  on the meridional plane at  $\theta = -0.5\pi$ , with the PIV error band.  $\Gamma = 7.81$ .

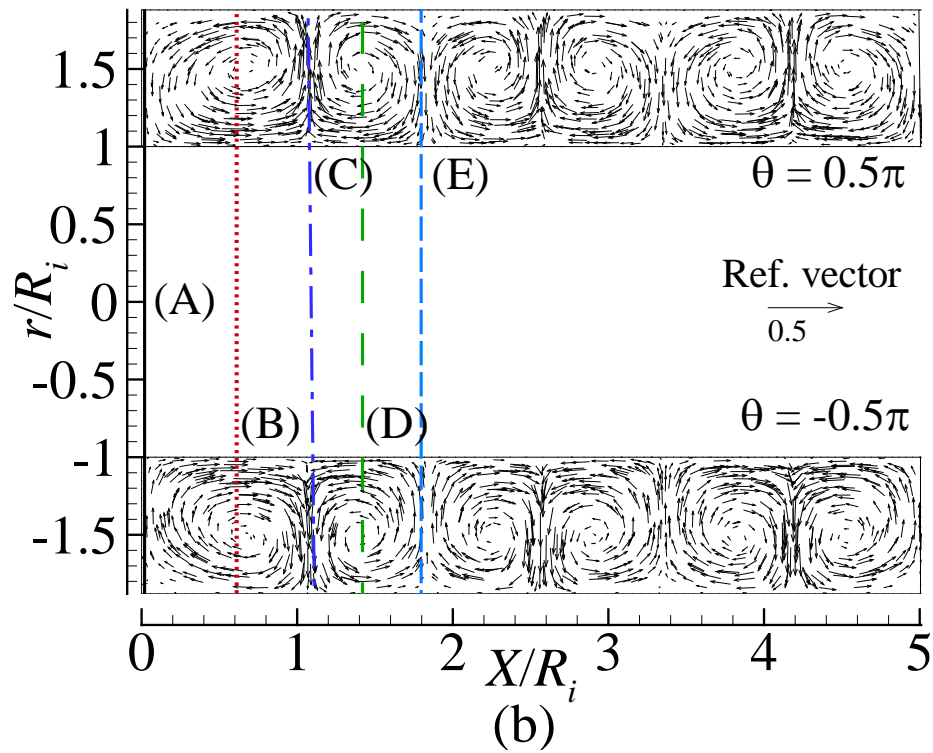
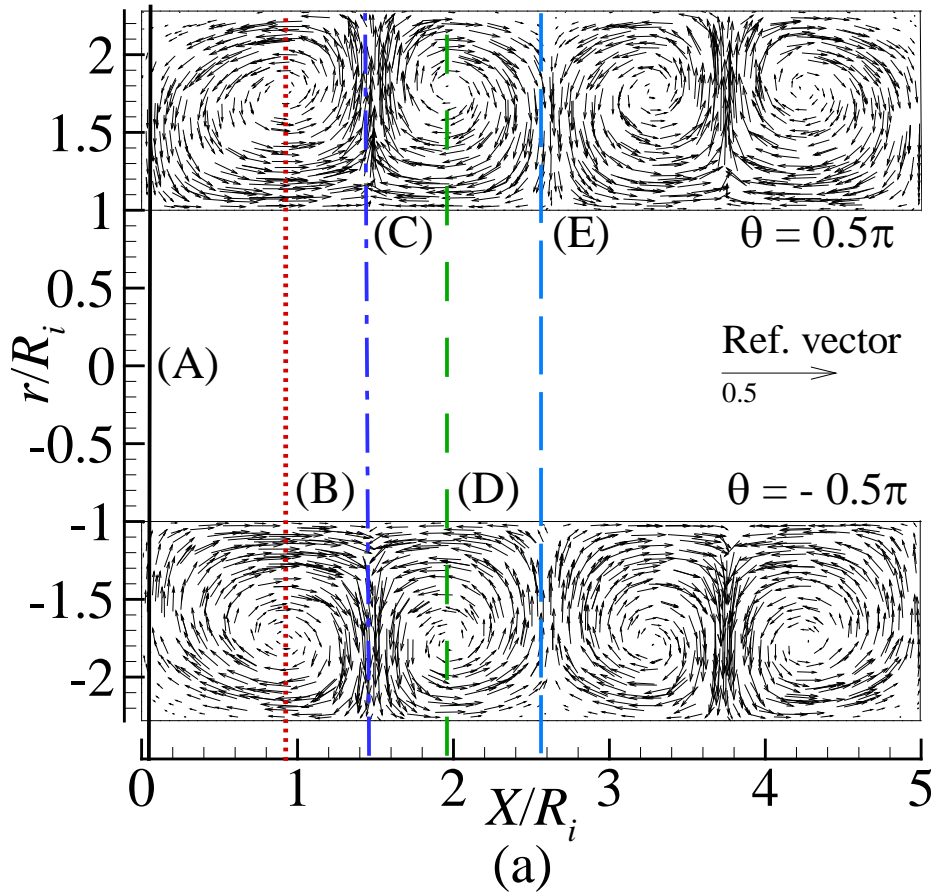


Fig. 4. Normalized velocity vectors in the meridional plane of the annulus for test cases (a)  $\Gamma = 7.81$  and (b)  $\Gamma = 11.36$ . The reference velocity vector is  $0.5\Omega R_i$ .

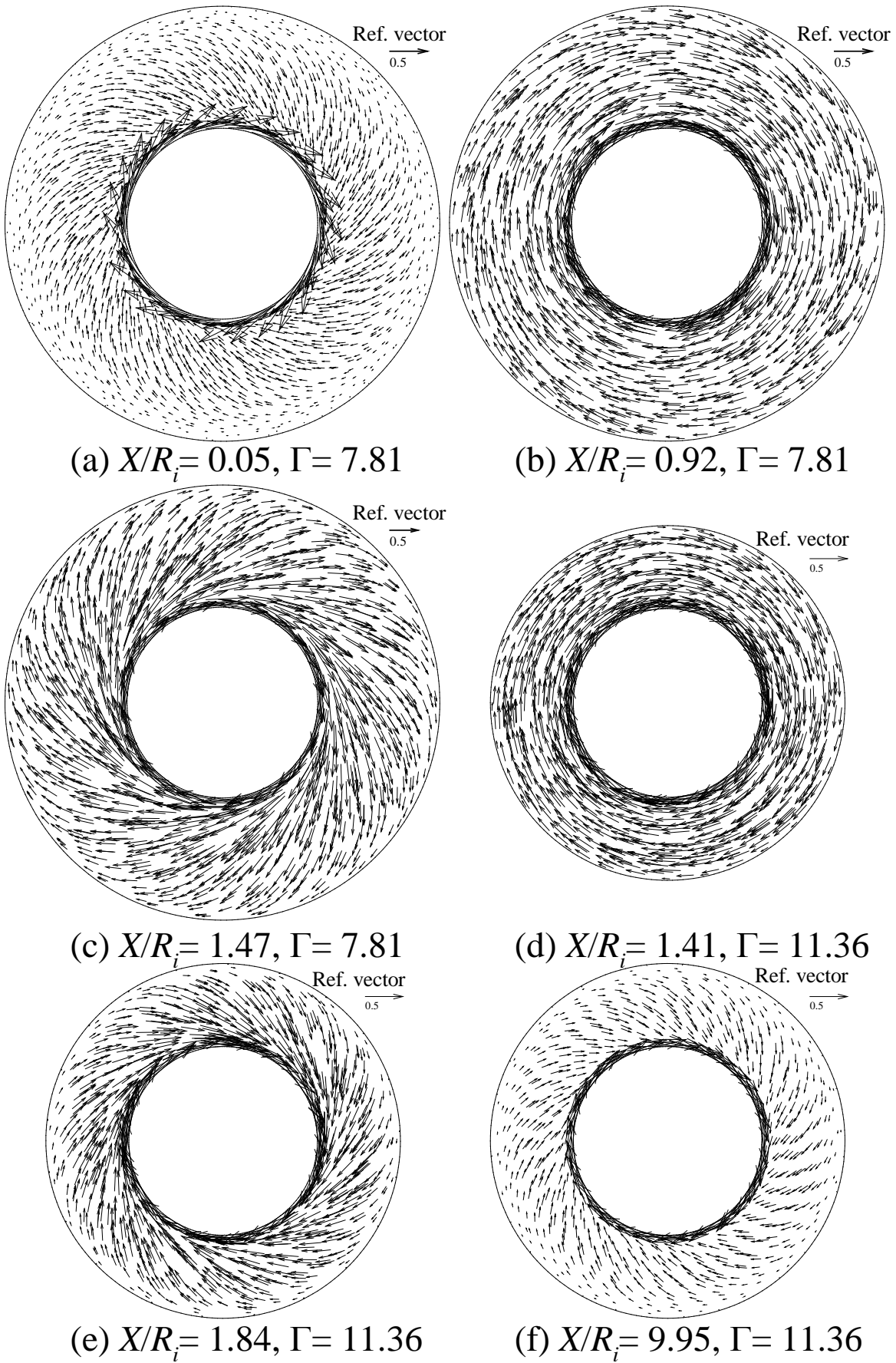
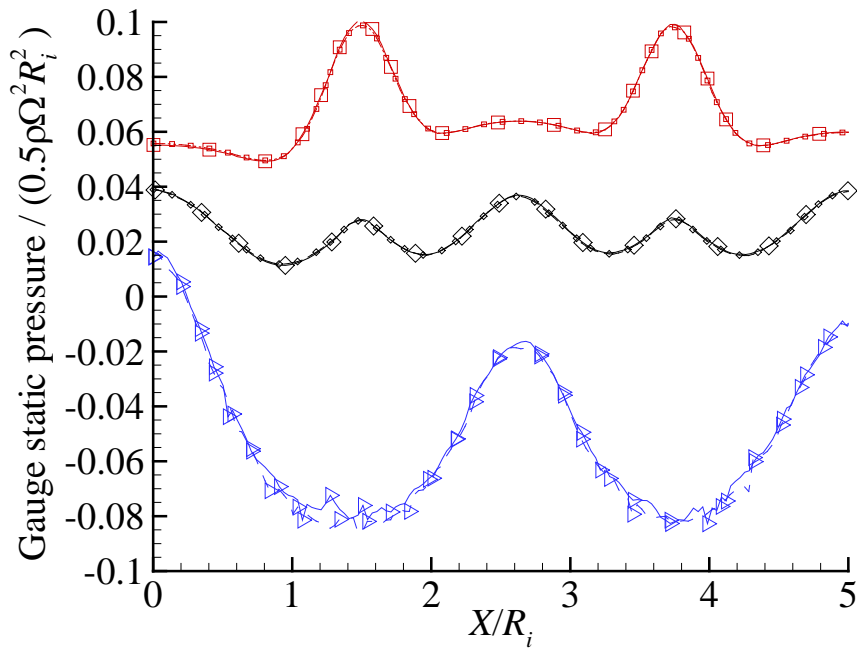
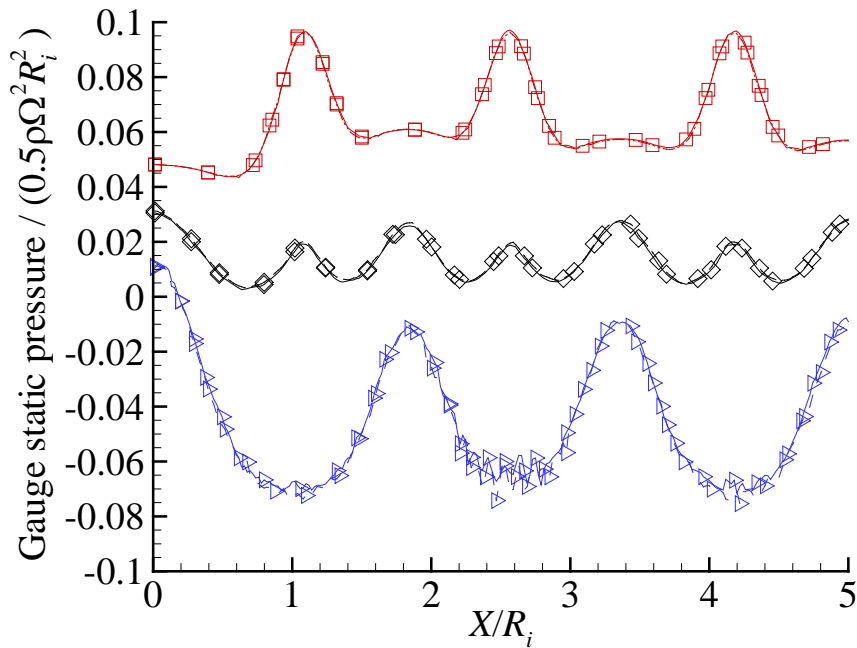


Fig. 5. Velocity vectors on different axial planes normalized by  $\Omega R_i$ .

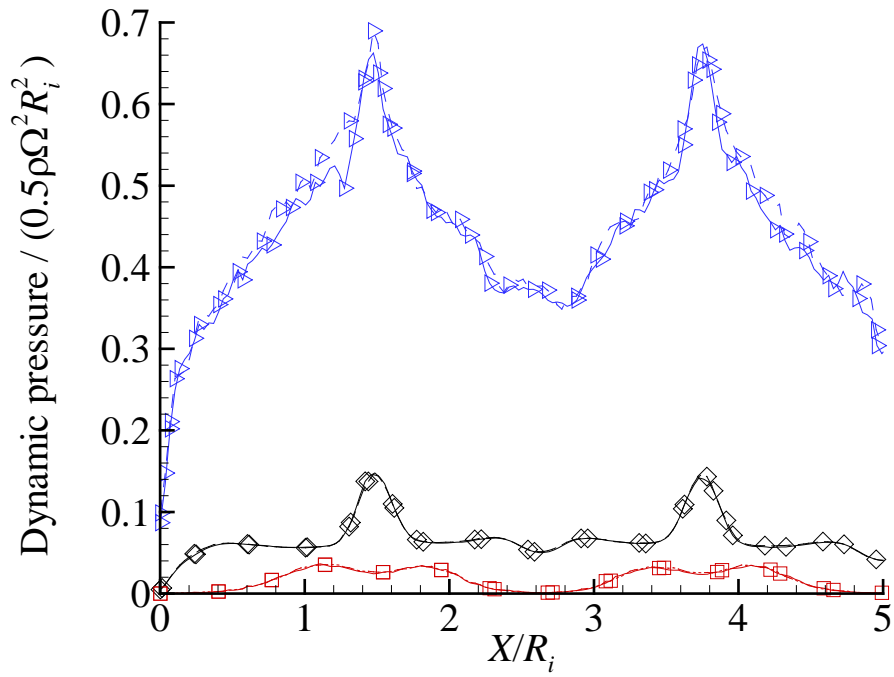


(a)

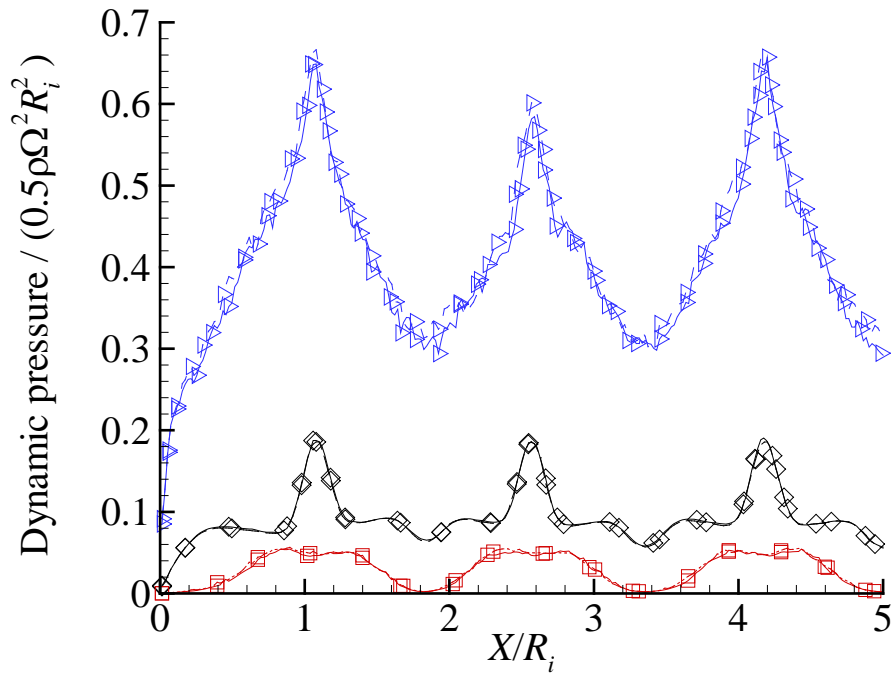


(b)

Fig. 6. Normalized gauge static pressure profiles in the meridional plane at constant radial positions ( $\triangleright$ )  $r = R_i + 0.045d$ , ( $\diamond$ )  $r = R_i + 0.500d$ , and ( $\square$ )  $r = R_i + 0.955d$  for the test cases (a)  $\Gamma = 7.81$  and (b)  $\Gamma = 11.36$ . (—)  $\theta = 0.5\pi$ , (---)  $\theta = -0.5\pi$ .



(a)



(b)

Fig. 7. Normalized dynamic pressure profiles in the meridional plane at constant radial positions, ( $\triangleright$ )  $r = R_i + 0.045d$ , ( $\diamond$ )  $r = R_i + 0.500d$ , and ( $\square$ )  $r = R_i + 0.955d$  for the test cases (a)  $\Gamma = 7.81$  and (b)  $\Gamma = 11.36$ . (—)  $\theta = 0.5\pi$ , (---)  $\theta = -0.5\pi$ .

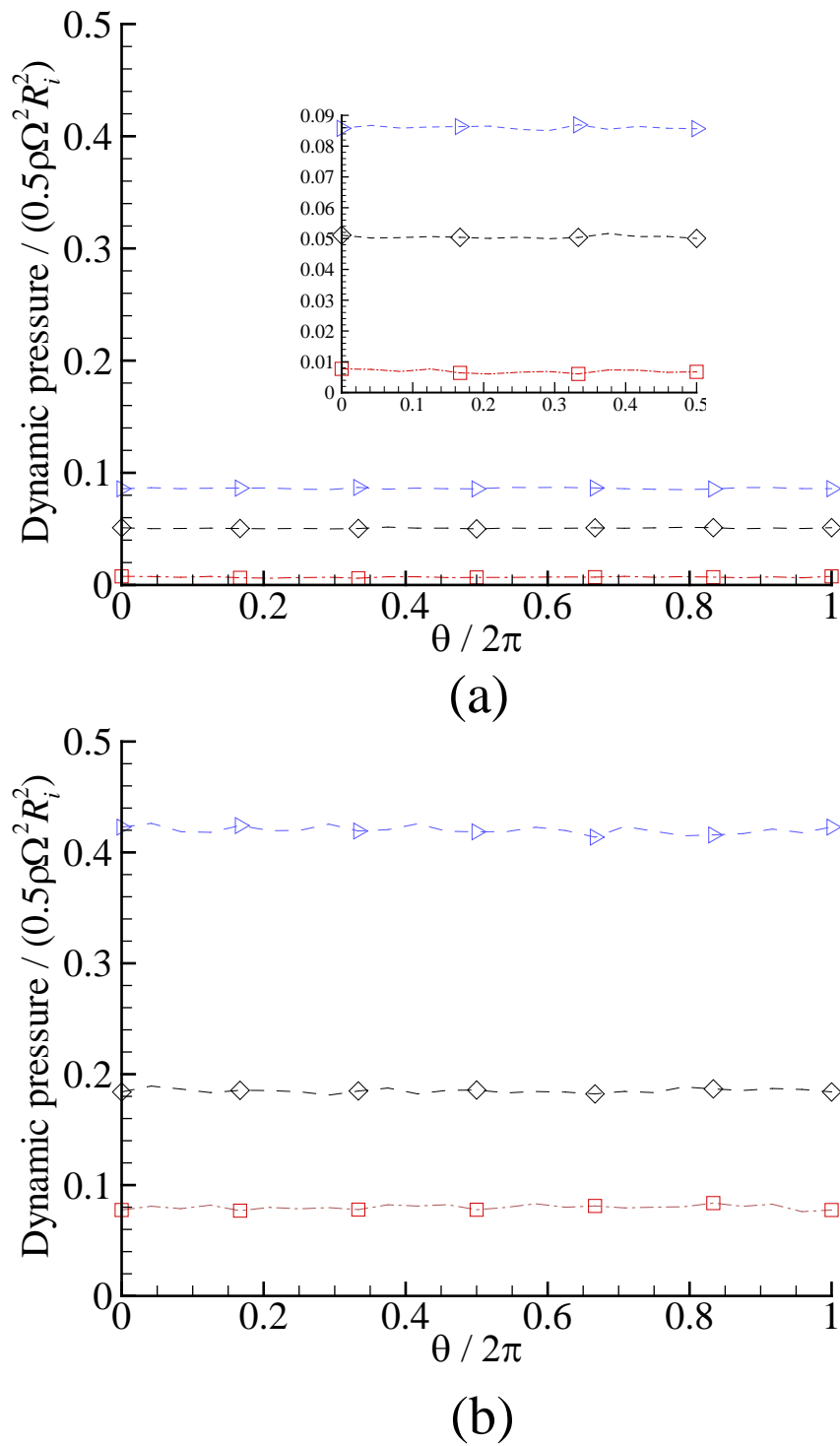


Fig. 8. Azimuthal profiles of normalized dynamic pressure at different radial heights on selected axial planes for the test cases (a)  $\Gamma = 7.81$  and (b)  $\Gamma = 11.36$ . ( $\triangleright$ )  $r = R_i + 0.045d$ , ( $\diamond$ )  $r = R_i + 0.500d$ , and ( $\square$ )  $r = R_i + 0.955d$ .

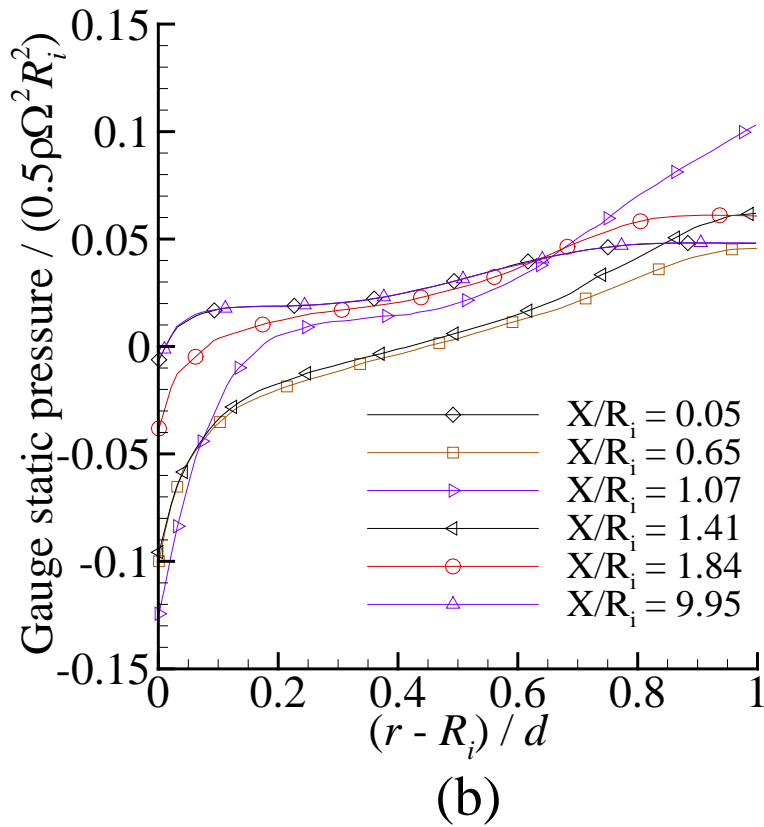
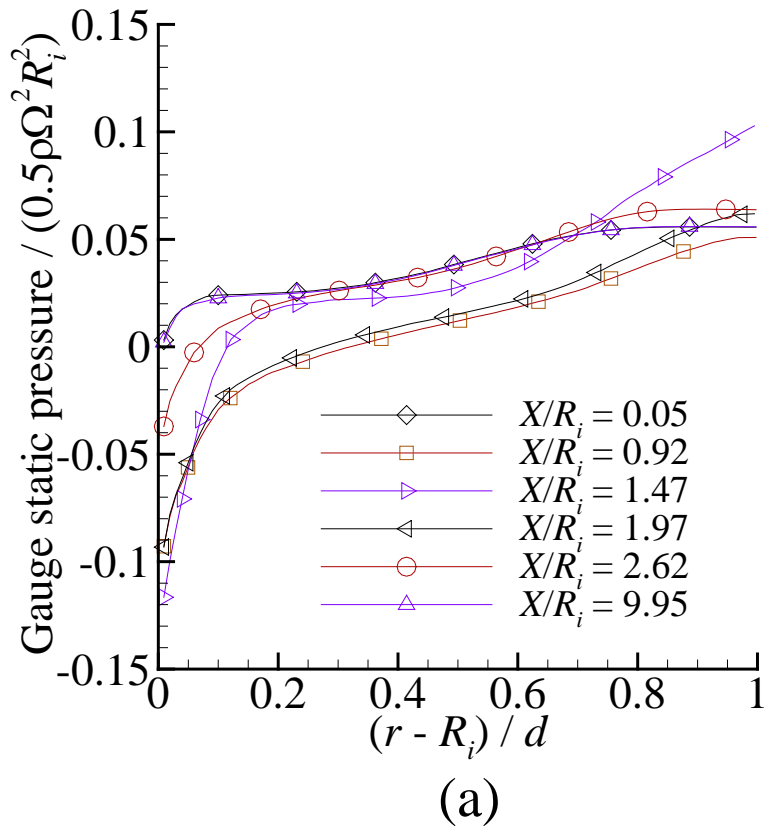
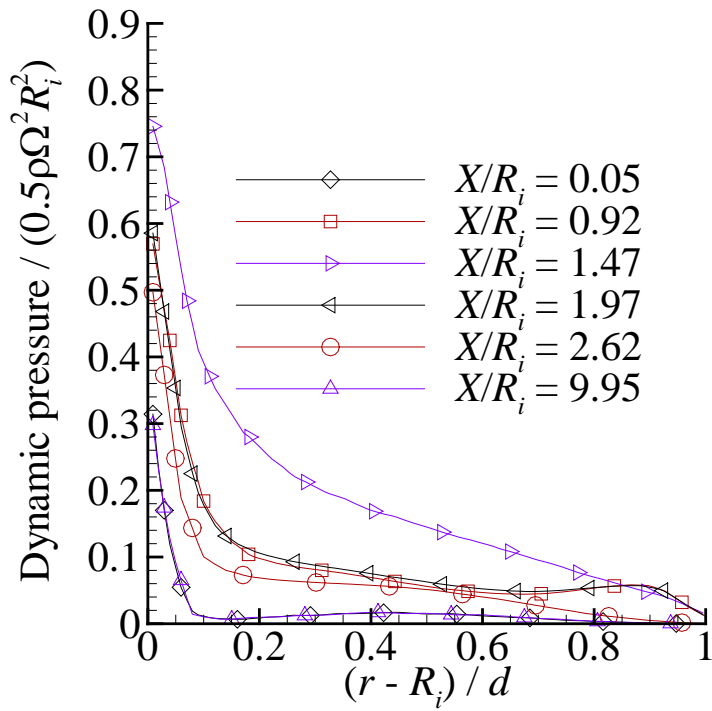
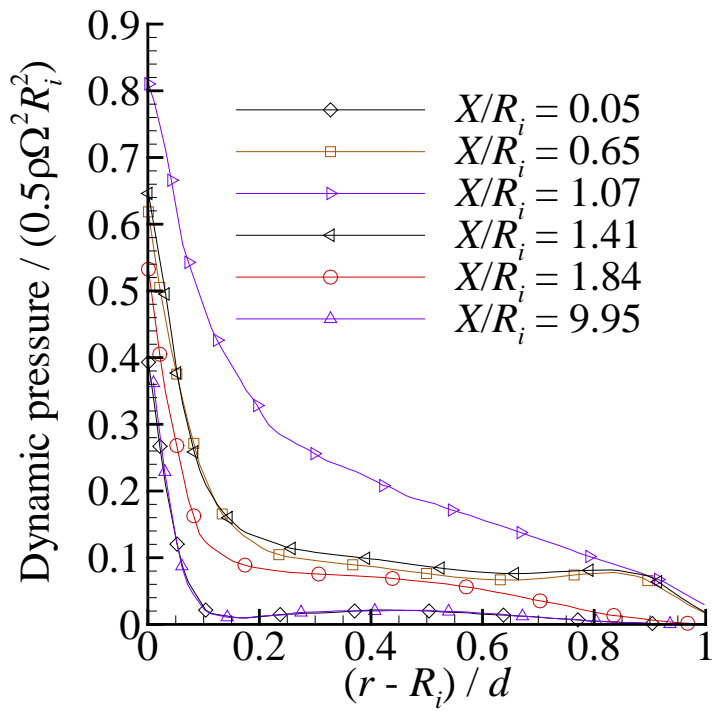


Fig. 9. Normalized gauge static pressure profiles on different axial planes at  $\theta = -0.5\pi$ ,

(a)  $\Gamma = 7.81$  and (b)  $\Gamma = 11.36$ .



(a)



(b)

Fig. 10. Normalized dynamic pressure profiles on different axial planes at  $\theta = -0.5\pi$ , (a)

$\Gamma = 7.81$  and (b)  $\Gamma = 11.36$ .

## Table Caption List

Table 1 Geometry of the test cases.

Description	Test case $\Gamma = 7.81$	Test case $\Gamma = 11.36$
Inner cylinder length (m)	0.25	0.25
Outer cylinder length (m)	0.25	0.25
Inner cylinder outer diameter (m)	0.05	0.05
Outer cylinder inner diameter (m)	0.114	0.094
Gap width $d$ (m)	0.032	0.022

Table 1: Geometry of the test cases.